



Virtuelle Triebwerksplattform (VirTriP): AP 4.2

CFD simulations of NG-Turb Inlet Volute and the Casings: Prüfstandssimulation NG-Turb

Berichtsnummer: DLR-IB-AT-GO-2022-142



Contents

List of figures	3
List of tables	3
1. Introduction	4
2. Motivation	4
3. Simulation Setup	4
3.1 Grid Convergence Index	5
4. Results	8
4.1 Issues with the simulation of whole setup	8
4.2 Solution for unphysical values	9
4.3 Overview of flow field	10
4.4 Overview of temperature field and HTC description	11
4.5 Comparison of temperature dent with measurements	11
5. Further Work	13
Bibliography	14
Appendix A	14

List of figures

Figure 1 NG-Turb test stand at AT-TUR.	4
Figure 2 Volute configuration with the casing and struts.	5
Figure 3 Structured grid of the configuration with the sector model for GCI.	6
Figure 4 Nusselt number (right) and temperature (left) distribution on the struts.	6
Figure 5 Mid-Span Nusselt number on volute (left) and inlet (right) struts with GCI error bars.	7
Figure 6 Near-wall discretization with wall functions (right) and low-Re treatment (left).	9
Figure 7 Non-physical temperatures in the domain (higher than inlet total temperature).	9
Figure 8 Flow and thermal fields in the plane $X = -0.37$	10
Figure 9 Flow and thermal fields in the plane $Y = 0$	10
Figure 10 Heat Transfer Coefficient distribution on the volute and the casings.	11
Figure 11 The plane of comparison (left) and propagation of temperature dent (right).	12
Figure 12 Temperature profiles in the plane $X = 1.405$ from the experiments and the simulations.	13
Figure 13 Settings for inlet panel.	14
Figure 14 Settings for outlet panel.	15
Figure 15 Solver settings.	15

List of tables

Table 1 Nusselt number errors obtained through the GCI.	7
--	---

1. Introduction

The Next Generation (NG)-Turb test facility is used for a detailed investigation of the turbine rigs with realistic conditions and flow parameters. It is aimed to couple the simulations and experiments by virtualizing the test stands. This enables the benefits of validation of the simulation processes and the minimization of experimental test rigs usage by providing a complementary understanding of the flow behavior. The usage of the test rigs can therefore be optimized which would lead to efficient utilization of time and costs.

2. Motivation

The NG-Turb inlet volute and test rig shown in figure 1 operate on higher temperatures which requires optimization of the duration of its usage. The inlet and volute struts undergo high thermal stresses due to elevated differences between the temperatures of the operating fluid and the test rig components. The measurement campaigns from the project HittTurb revealed a temperature dent at the inlet to the turbine in the test rig. The goal of the current work is therefore classified as follows,

1. To obtain the heat transfer coefficients on the inlet volute, the struts, and the casings of the rig. The results would be further used in thermomechanical analysis and possible redesigning of the struts, depending on the thermal stresses obtained from various operating conditions.
2. The presence of the temperature dent at the turbine inlet has a significant effect on the calculation of the efficiency in the turbine rig. Therefore, the dent is to be identified through the simulations and its location should be approximately compared to that of the experiments.

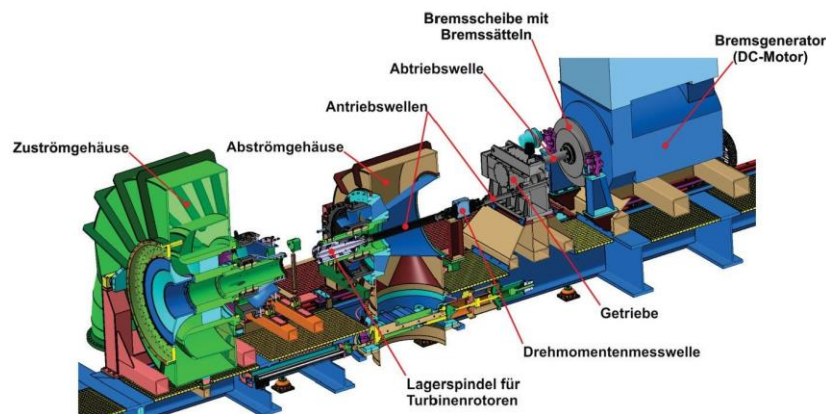


Figure 1 NG-Turb test stand at AT-TUR.

An approach to address the above issues can be represented as follows: The determination of heat transfer coefficients is highly grid refinement-dependent [1]. Therefore, an initial sector model (45°) is chosen to analyze the grid refinement requirements, and the complete setup is then simulated considering the required refinement level of spatial discretization.

3. Simulation Setup

The steady RANS simulations of the volute configuration (shown in figure 2) are performed using in-house CFD code TRACE (version 9.4.1), developed by AT-NUM [2]. The working fluid is considered to be an ideal gas

with a gas constant of $R = 287 \text{ J/kgK}$ and a specific heat ratio of $\gamma = 1.4$. The viscosity of the fluid is modeled with Sutherland's law of viscosity and the Prandtl number equals 0.71. All the simulations are performed using the Menter SST 2003 turbulence model [3] and the turbulent scalar flux modeling is performed based on the Reynolds analogy, for a constant turbulent Prandtl number of 0.9.

The boundary conditions are taken from the measurement campaign, where the inlet is assigned a total pressure of 159 kPa and a total temperature of 450 K. The solid walls of the configuration are treated as viscous (no-slip) walls with an isothermal boundary condition of 300 K. The desired mass flow rate at the outlet was 3.29 kg/s, which resulted in a bulk Mach number ≈ 0.01 in the volute. The Riemann boundary condition is intended to be an appropriate boundary condition type for the current configuration. This allows input of velocity and pressure 2D-distributions at the inlet. However, the 2D input along with the Riemann boundary resulted in a divergence of the solution. This issue was resolved by the deactivation of modification of the boundary values to match the specified parameters (e.g. total or static pressure, mass flow rate etc.). The following command for the inlet and outlet panels is added in the control file. The solver settings along with the boundary condition treatment in GMC is shown in the Appendix A.

"-COMPUTE_RIEMANN_INVARS_DIRECTLY_FROM_BD_VALUES"

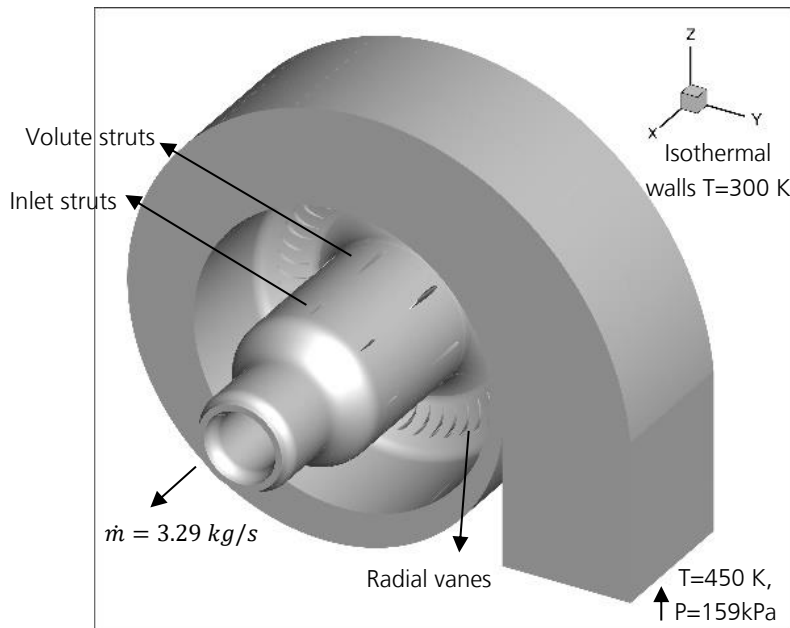


Figure 2 Volute configuration with the casing and struts.

3.1 Grid Convergence Index

The structured grid shown in figure 3 is generated using PyMesh for the struts and the casing. An existing G3DMesh template was used for the inlet volute mesh generation. A grid convergence study is performed on the sector models of the struts for an initial estimation of the grid requirements for an appropriate heat transfer coefficient computation. The Grid Convergence Index (GCI) [4] based on Richardson's extrapolation is used to address the errors arising purely from the computational mesh sizes. It is one of the standardized methods to analyze the dependence of the numerical solution on spatial discretization. The GCI error is calculated by

considering the absolute errors of parameters for different grids and the level of refinement amongst the grids. Three different grids are obtained by doubling the total elements in the domain through each level of refinement. All the grids have been generated considering the requirement of a low-Reynolds turbulence model where the average near-wall dimensionless distance (y_1^+) in the domain is maintained to be lesser than 2 and uniform refinement of surface and the volumetric elements is ensured.

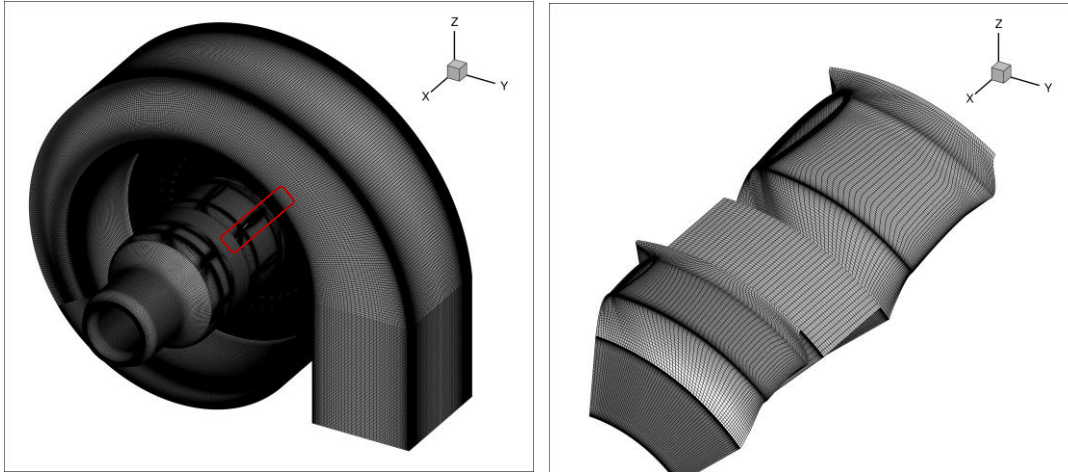


Figure 3 Structured grid of the configuration with the sector model for GCI.

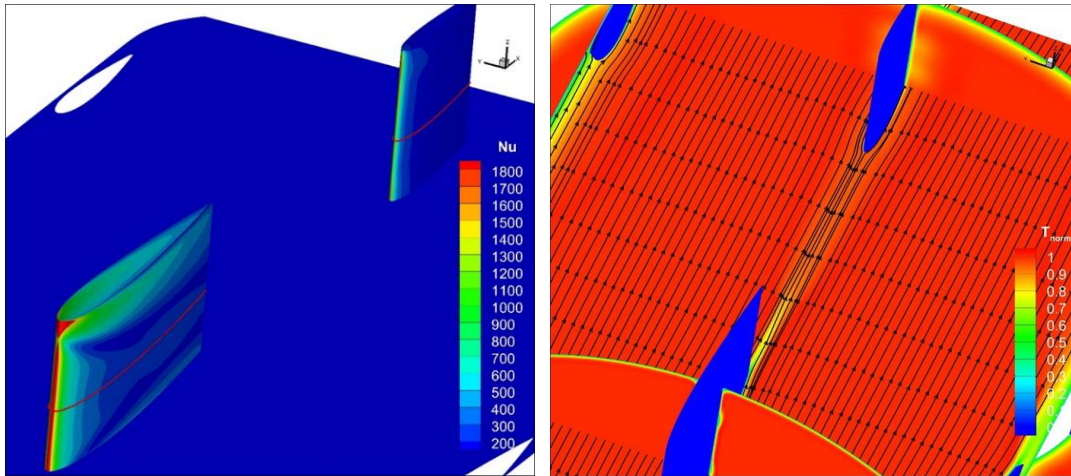


Figure 4 Nusselt number (right) and temperature (left) distribution on the struts.

As seen in figure 4, the highest heat transfer rates are obtained in the stagnation regions of the struts. The Nusselt number at the mid-span of the struts (marked with red line) is considered a parameter for the GCI study. The Nusselt number is a non-dimensional heat transfer parameter and is calculated as a ratio of convective to conductive heat transfer at the walls. It is calculated as follows,

$$Nu = \frac{\dot{q}_w l}{k_f (T_w - T_{ref})}$$

where, k_f is the thermal conductivity of the fluid and \dot{q}_w , T_w are the heat flux and the temperature at the wall respectively. The T_{ref} here is the adiabatic wall temperature and the l is the respective chord length of the struts.

The Nusselt number distributions obtained for three grids at the mid-span of the struts are shown in figure 5. The error bars are obtained through GCI of the fine grid and indicate a 95% certainty of the Nusselt number lying in the region of the ideal solution. Table 1 shows the maximum and median errors obtained on the struts. Large deviations are obtained in the stagnation region. This zone exhibits sensitivity in the calculation of HTC's to the near-wall spatial discretization. As the fine and intermediate grids exhibit minor variations, the intermediate grid and its related parameters are chosen for further meshing of the components.

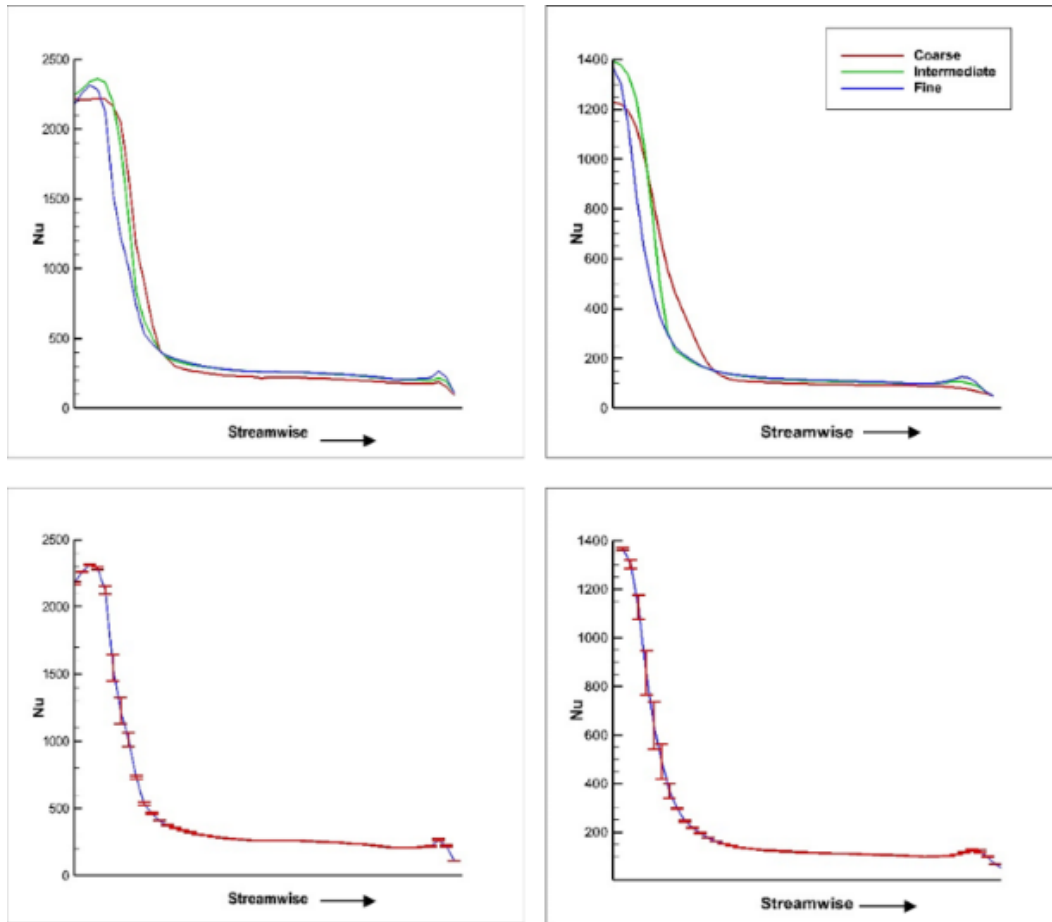


Figure 5 Mid-Span Nusselt number on volute (left) and inlet (right) struts with GCI error bars.

GCI Fine	Volute Strut	Inlet Strut
Maximum error %	8	15
Median error %	0.244	0.726

Table 1 Nusselt number errors obtained through the GCI.

4. Results

4.1 Issues with the simulation of whole setup

The complete configuration was simulated till the desirable convergence was achieved and the fluctuations of the mass flow rate at the outlet dropped to the order of 10^{-7} . TRACE is a flow solver for compressible flows. An appropriate adaptation of this solver to incompressible flows (with a bulk Mach number of ≤ 0.2) requires the usage of low-Mach preconditioning [5]. This reduces the stiffness of the system and results in higher accuracy of the flow solution with faster convergence. TRACE allows the usage of constant preconditioning parameter β and also locally varied parameters l and k . However, the implementation of low-Mach preconditioning with various parameters in the current configuration led to divergence of the solution. Therefore, the preconditioning was avoided, resulting in the requirement of higher iterations for a convergence of the flow solution.

The simulations resulted in large deviations and discontinuities of the velocity, pressure, and temperature distributions in the volute. The reason was estimated to be the relatively larger differences in the refinement levels of spatial discretization. The grid refinement is vastly varied in the domain due to multiple components of various dimensions. This also resulted in large separation zones at the location of 90° flow turn after the radial vanes.

The thermal boundary layer in the volute revealed temperature values higher than the inlet total temperature (450 K), shown in figure 7. Considering the configuration is stationary and no work has been done on the fluid, these higher values are unexpected and unphysical. This behavior of the flow solution was also initially associated with the non-uniform grid in the components. Therefore, the configuration was re-meshed in order to maintain a nearly-constant grid density and mesh cell sizes in the domain.

The requirement of a uniform grid in the domain resulted in a large grid of about 60M elements in total satisfying the low-Re criterion of $y_1^+ \leq 2$. In order to reduce the no. of wall functions may be considered to resolve the near-wall thermal and velocity boundary layers. Figure 6 shows the reduction of near-wall discretization variation through the usage of wall functions on the inlet strut. This has resulted in a total reduction of cell count to 12M in the domain. The wall functions allow the usage of grids of up to $y_1^+ > 30$ thereby, resulting in a significant reduction of total cell count. It is required for the first mesh cell to be placed in the log-law region of the boundary layer. The viscous region is therefore resolved using the empirically derived equations. Although a well-resolved boundary layer is crucial for the accurate calculation of HTC's, the application of wall functions is a reasonable choice in the current configuration as they result in sufficient accuracy in two-dimensional flows without separations [6]. Therefore, spalding wall functions and isothermal wall functions implemented in TRACE are considered to model the near-wall velocity and thermal profiles respectively.

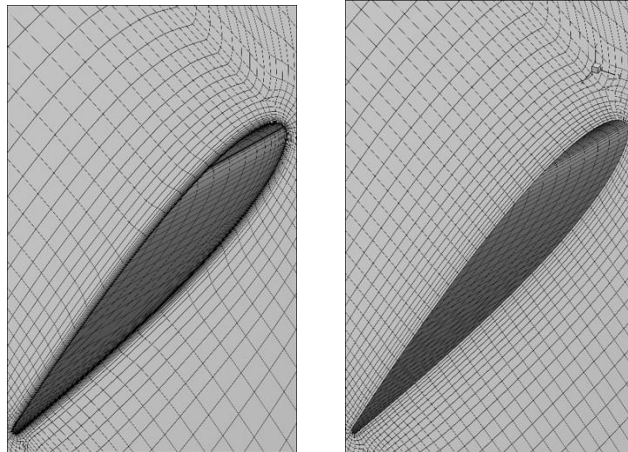


Figure 6 Near-wall discretization with wall functions (right) and low-Re treatment (left).

The comparison of low-Re and the wall functions resulted in a similarity of the velocity fields in the domain. However, the issue of non-physical temperature results is amplified. The wall functions also resulted in larger separation zones at the region of flow bending and therefore the usage of wall functions was not considered further.

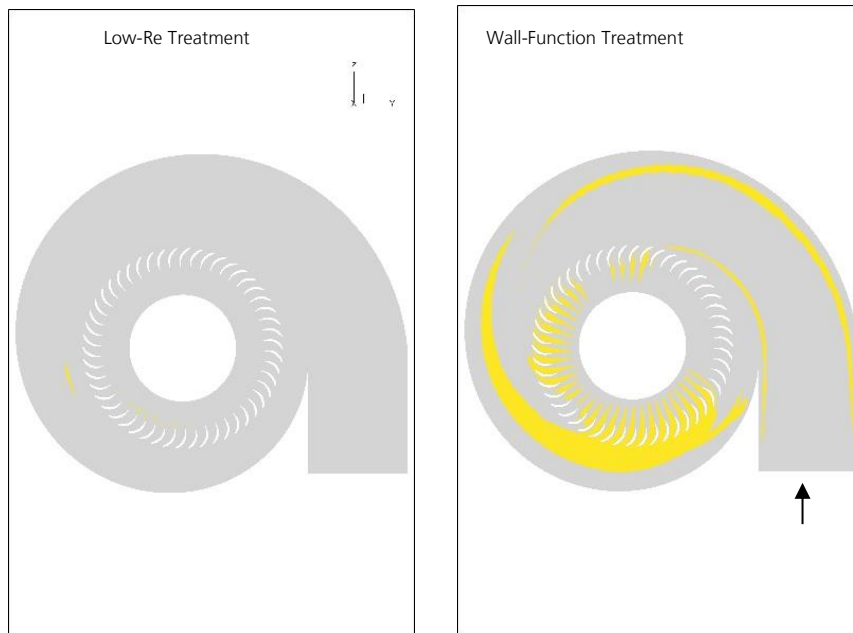


Figure 7 Non-physical temperatures in the domain (higher than inlet total temperature).

4.2 Solution for unphysical values

The unphysical temperature values were found to be independent of the near-wall grid resolution, the turbulence model used, or the type of boundary conditions assigned to the inlet and the outlet. Although a constant temperature is assigned to the inlet boundary panel, the higher temperatures seem to arise from the inlet itself and then propagate in the fluid domain. It was found that the issue arises due to the usage of the VanAlbaDaSqr limiter in the structured grid, resulting in overshoots and undershoots of the temperature. Therefore,

the limiter was switched to VanAlbada which resulted in meaningful temperature distributions, thereby resolving the issues of unphysical results.

4.3 Overview of flow field

The flow enters the domain in the +Z direction (shown in figure 8) and travels further in the volute with a decreasing cross-sectional area. The velocity of the flow increases as the flow approaches the radial vanes where a smooth perpendicular bending in the +X-direction is experienced. Separation zones are formed at the regions of flow turning after the radial vanes. As seen in figure 9, the streamlines indicate a reattachment after a distance of 0.023 m in the axial direction. The flow then exhibits a nearly two-dimensional behavior where the velocity of the flow again increases as the cross-sectional area reduces.

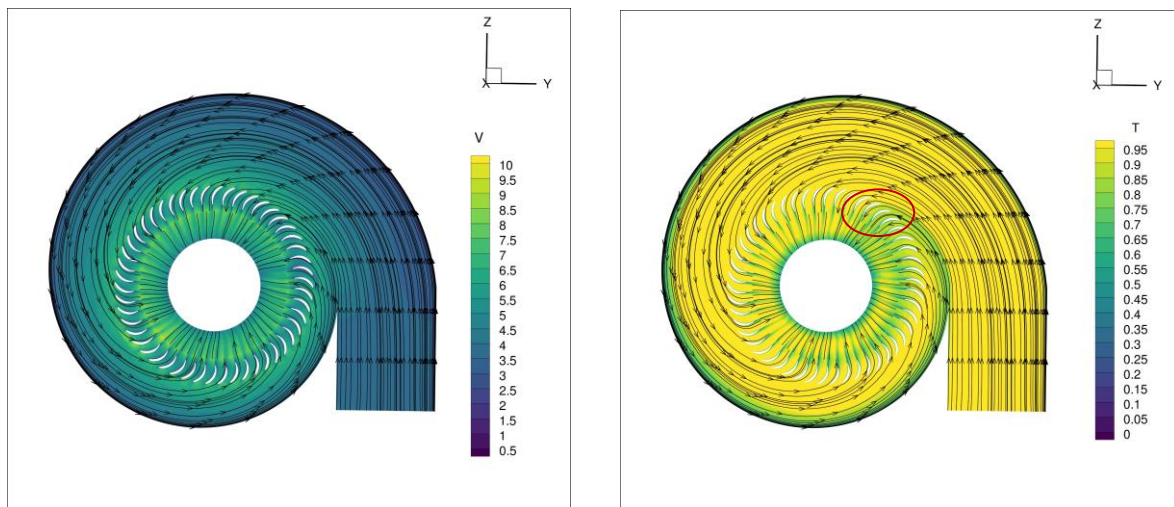


Figure 8 Flow and thermal fields in the plane $X = -0.37$.

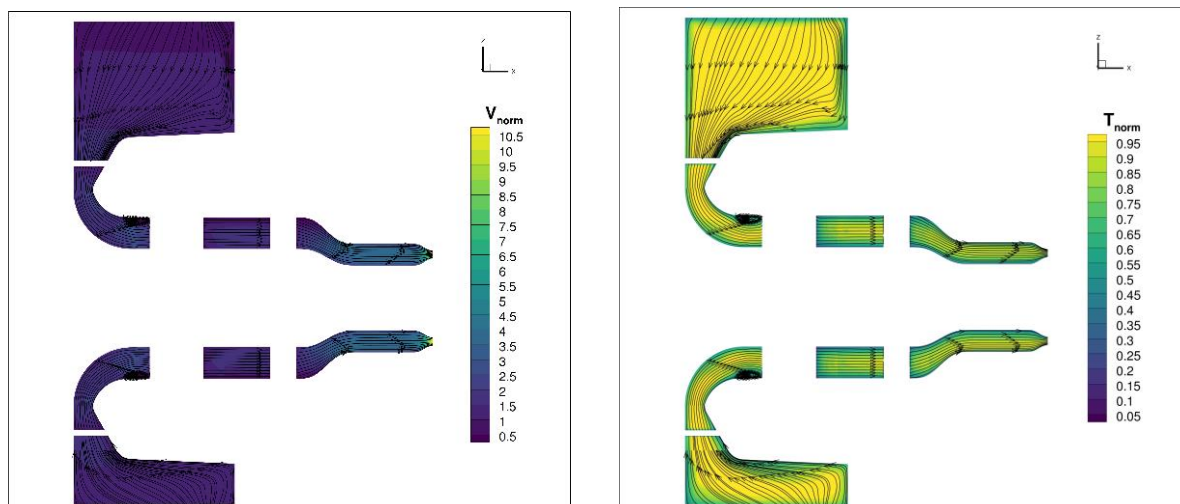


Figure 9 Flow and thermal fields in the plane $Y = 0$.

4.4 Overview of temperature field and HTC description

The thermal boundary layers increase in thickness as the flow travels towards the radial vanes. This indicates high heat transfer rates at the inlet region of the domain and lower HTC as the temperature difference between the inlet volute and the fluid reduces. High heat transfer regions are obtained in the stagnation regions of the radial vanes, the volute, and the inlet struts where the flow impinges. As a result of heat transfer between the fluid and the struts at lower temperatures, the fluid temperature in the wakes of the struts is reduced. The separation zones at the flow turning region results in poor heat transfer areas followed by elevated heat transfer rates due to the reattachment of the flow. These regions are subjected to high thermal stresses due to large heat fluxes. A temperature deficit zone is noticed in the area of flow being bent towards the radial vanes. This results in non-axisymmetric distribution of temperature of the flow traveling in the axial direction. This is found to be the origin of the temperature dent that propagates to the turbine inlet. The HTC distribution on the casing along with the struts is shown in figure 10 and is calculated as:

$$HTC = \frac{\dot{q}}{T_{aw} - T_{fluid}}$$

where, q is the heat flux at the wall and the T_{aw} is adiabatic wall temperature.

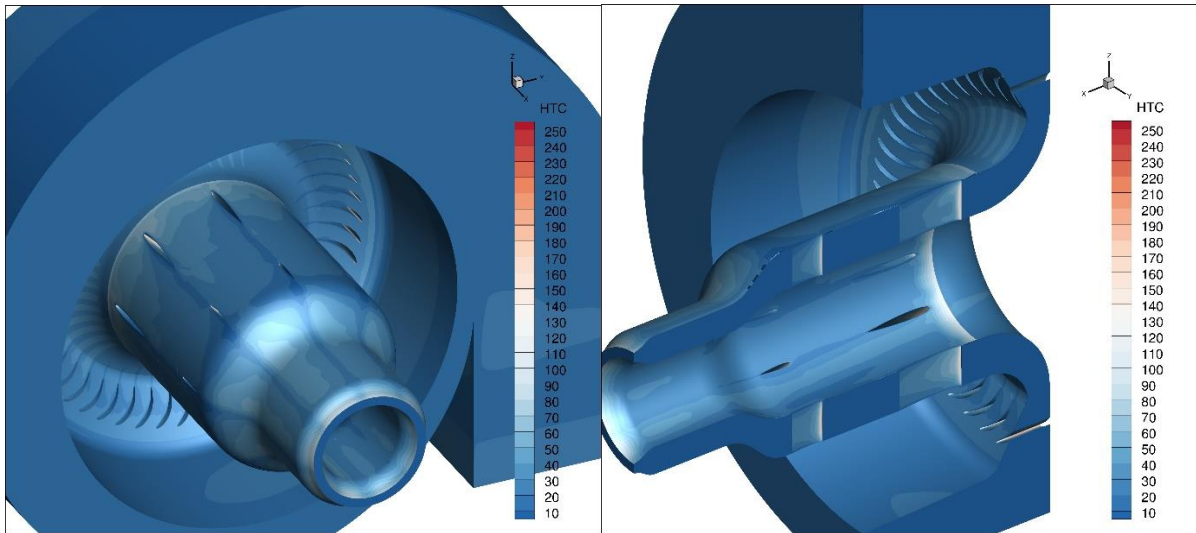


Figure 10 Heat Transfer Coefficient distribution on the volute and the casings.

4.5 Comparison of temperature dent with measurements

Figure 11 shows the temperature distribution in the plane $X = 1.405$. This plane was chosen to compare and quantify the dent found in the experiments. A one-to-one comparison of the dent is not possible due to the differences in the operating conditions and the boundary conditions between the experiments and the simulations. The non-uniformities in the temperature distribution arise here due to two reasons. The heat transfers due to the interaction of the fluid with the set of struts resulted in regions of lower temperature in the wake regions. An additional temperature deficit zone can be noticed at the location of $270^\circ < \alpha < 360^\circ$ due to the bending of the flow from the volute to the radial vanes. The angle α is measured from the positive Z-axis in the clockwise direction, while looking in the +X direction. The temperature shown is non-dimensionalized as follows,

$$T_{norm} = \frac{(T - T_{solid})}{(T_{inlet} - T_{solid})}$$

where the parameters are: $T_{inlet} = 450 \text{ K}$, $T_{solid} = 300 \text{ K}$ and $T_{inlet} \approx 460 \text{ K}$, $T_{solid} \approx 408 \text{ K}$ for the simulations and the experiments respectively.

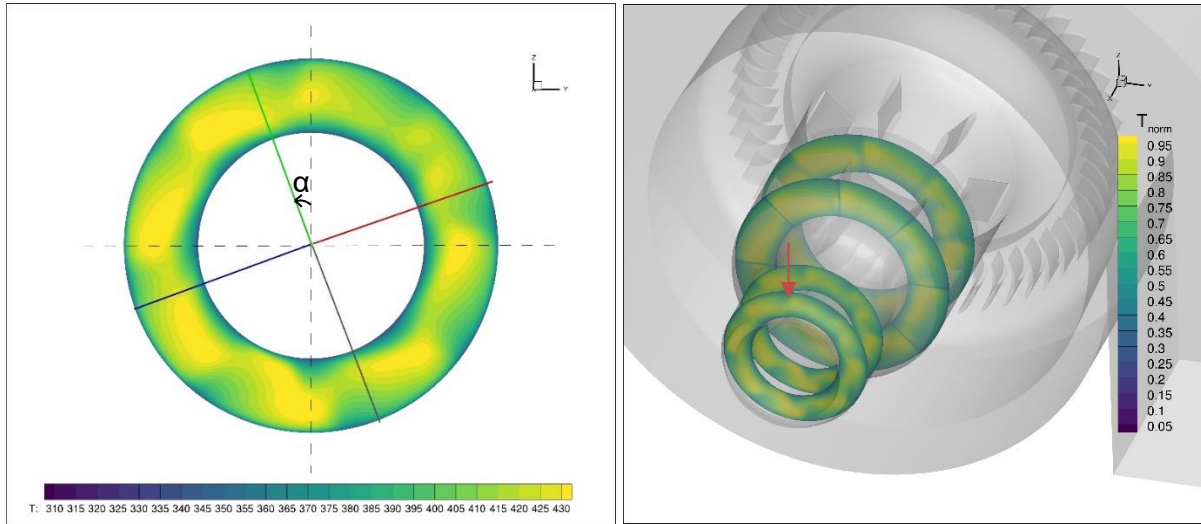


Figure 11 The plane of comparison (left) and propagation of temperature dent (right).

The total temperature variation in various circumferential locations from the simulations and the experiments are plotted in figure 12. The dotted lines represent the measurement data whereas the solid ones denote the profiles extracted from the simulations at the corresponding locations. The measurement data was available for four different circumferential locations in the plane $X=1.405$. The plot shows normalized temperature plotted against the radius. The simulation results show a qualitative similarity with the measurement data where lower values are obtained at a location of 292.5° . However, the slopes of the temperature curves are more pronounced in the simulations. A more accurate comparison can be made with additional measurement points and similar boundary temperature values.

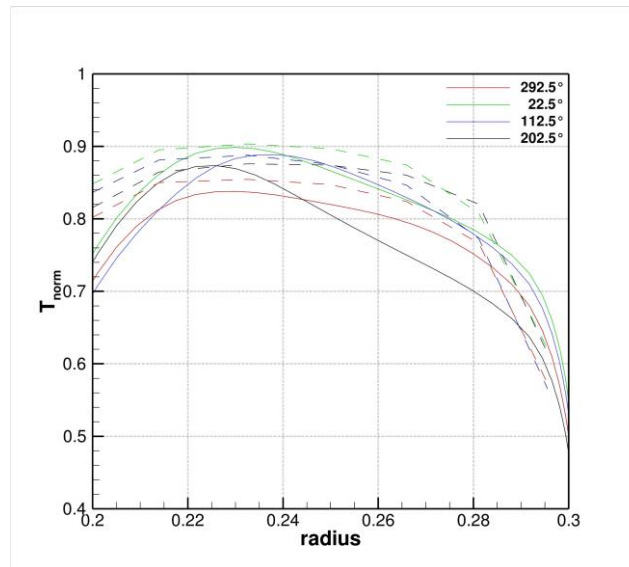


Figure 12 Temperature profiles in the plane $X = 1.405$ from the experiments and the simulations.

5. Further Work

The obtained HTC's on the struts and the casings of the volute can be used further for a thermo-mechanical analysis to identify the regions undergoing high thermal stresses. The current work involves a comparison of thermal profiles from the measurements to that of the simulations in a single plane. The further work to improve this comparison can be listed as follows,

1. A detailed validation of the temperature distributions obtained and more accurate dent location can be made with a larger set of measurement data.
2. An FSI simulation with the consideration of conduction in the solid would enable a closer comparison of the measurements and the simulations. An existing option for this could be the coupling of TRACE with the FEM solver CalculiX.
3. The current RANS simulations required about 60000 iterations leading to the flow solution residuals dropping to 10^{-8} . Therefore, to obtain faster convergence, low-Mach preconditioning with suitable parameters may be considered.
4. Additionally, it would be interesting to simulate the current configuration for various thermal and flow boundary conditions to analyze the variation of the temperature dent and its effect on the efficiency calculation.
5. The geometry of the configuration may be varied to a realistic one to take into consideration the effect of details such as flow grid and flow straightener on the flow and thermal fields.

Bibliography

- [1] A. R. B. W. Julia Wienand, "Numerical study of a turbulent impinging jet for different jet-to-plate distances using two-equation turbulence models," *European Journal of Mechanics - B/Fluids*, Vols. Volume 61, Part 2, no. ISSN 0997-7546, pp. Pages 210-217, 2017.
- [2] K. & H. K. & K. E. Becker, "Recent Progress In A Hybrid-Grid CFD Solver For Turbomachinery Flows," *V European Conference on Computational Fluid Dynamics ECCOMAS CFD*, no. 978-989-96778-1-4, 2010.
- [3] F. a. K. M. a. L. R. Menter, "Ten years of industrial experience with the SST turbulence model," *Journal of Heat and Mass Transfer*, vol. 4, 2003.
- [4] P. J. Roache, "Perspective: A Method for Uniform Reporting of Grid Refinement Studies," *Journal of Fluids Engineering*, vol. 116, no. 0098-2202, pp. 405-413, 1994.
- [5] http://www.trace-portal.de/userguide/trace/page_lowMachPreconditioning.html.
- [6] B. S. A. S. M. B. S. a. Č. S. Stankovic, "Evaluation and limitations of standard wall functions in channel and step flow configurations," *Journal of the Serbian Society for Computational Mechanics*, vol. 8, pp. 1-22, 2014.

Appendix A

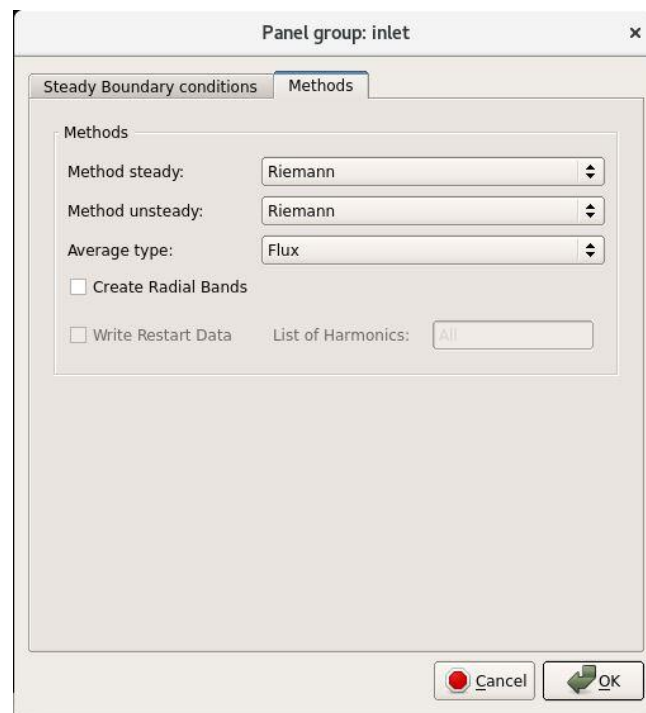


Figure 13 Settings for inlet panel.

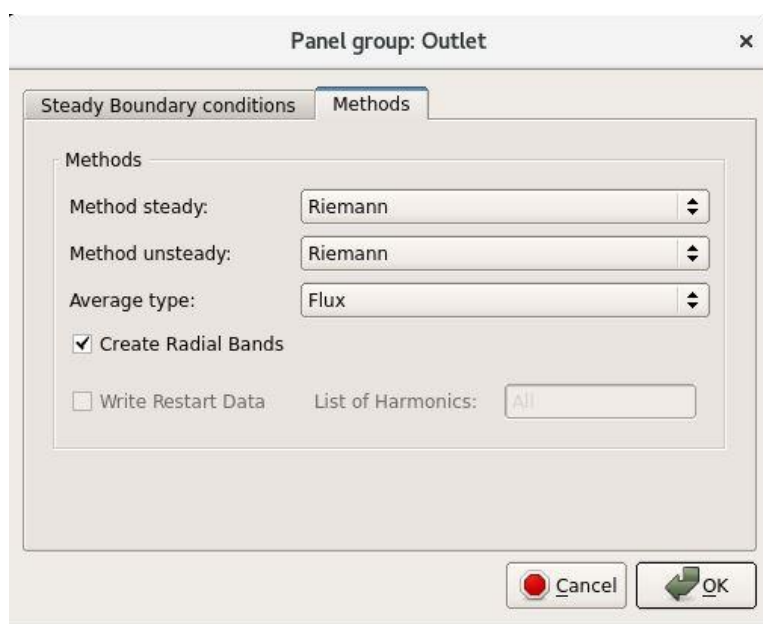


Figure 14 Settings for outlet panel.

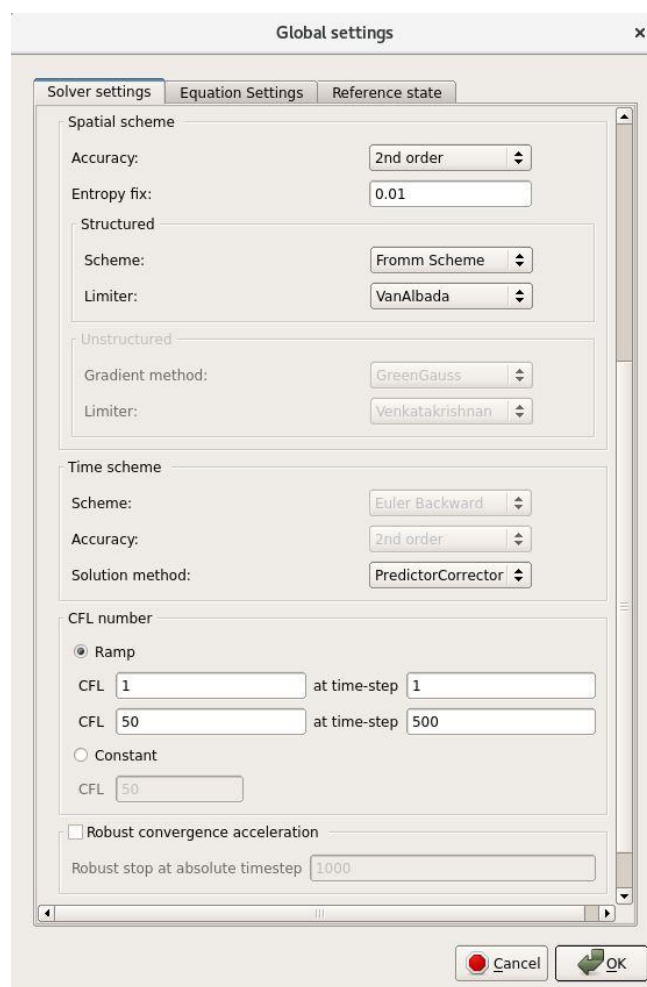


Figure 15 Solver settings.